Ultrasensitive dual-enhanced sandwich strategy for simultaneous detection of *Escherichia coli* and *Staphylococcus aureus* based on optimized aptamers-functionalized magnetic capture probes and graphene oxide-Au nanostars SERS tags

Wenshi Zhao [a,b,c], Shuo Yang [d], Daxin Zhang [a,b,c], Tianxiang Zhou [a], Jie Huang [a], Ming Gao [a], Yuhong Jiang [a], Yang Liu [a,*], Jinghai Yang [a,*]

[a] *Key Laboratory of Functional Materials Physics and Chemistry (Ministry of Education), College of Physics, Jilin Normal University, Changchun 130103, China*
[b] *Changchun Institute of Optics, Fine Mechanics and Physics, Chinese Academy of Sciences, Changchun 130033, China*
[c] *University of Chinese Academy of Sciences, Beijing 100049, China*
[d] *College of Science, Changchun University, Changchun 130022, China*

HIGHLIGHTS

- A SERS platform for simultaneous detection of *E. coli* and *S. aureus* was developed.
- A dual SERS enhancement strategy based on sandwich-like structure was applied.
- Aptamers modified-Fe$_3$O$_4$@SiO$_2$-Au NCs were used for bacterial capture and isolation.
- GO-Au NSs functionalized with DTNB/4-MBA and aptamers were proposed as SERS tags.
- The detection limit for *E. coli* and *S. aureus* was as low as 10 cfu/mL.

GRAPHICAL ABSTRACT
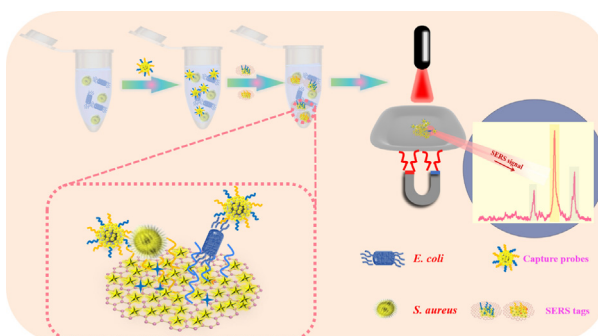
ARTICLE INFO

ABSTRACT

In this work, a novel surface-enhanced Raman scattering (SERS) sandwich strategy biosensing platform has been established for simultaneously detecting *Escherichia coli* (*E. coli*) and *Staphylococcus aureus* (*S. aureus*). Fe$_3$O$_4$@SiO$_2$-Au nanocomposites (NCs) with varying amounts of Au nanocrystals were prepared, and the effect of interparticle gaps on SERS activity was studied by finite-difference time-domain (FDTD) method. The optimal magnetic SERS-active substrates (FS-A5) were functionalized with the specific aptamers to act as capture probes. Meanwhile, graphene oxide-Au nanostars (GO-Au NSs) decorated with Raman reporters and aptamers were used as SERS tags. The loading density of Au NSs on GO was tuned to change the number of SERS active sites. In this proposal, *E. coli* and *S. aureus* were first captured by capture probes and then bound with SERS tags to form a sandwich-like structure, which caused enhanced electromagnetic field because of the dual enhancement strategy. Under optimal conditions, SERS platform could detect *E. coli* and *S. aureus* simultaneously, and the detection limit was as low as 10 cfu/mL. Our sandwich assay-based dual-enhanced SERS platform provides a new idea for simultaneously detecting multiple pathogens with high selectivity and sensitivity, and thus will have more hopeful prospects in the field of food safety.

1. Introduction

Infectious diseases resulting from bacterial infections have posed a huge threat to global public health [1–3]. Among the known pathogens, *Escherichia coli* (*E. coli*) and *Staphylococcus aureus* (*S. aureus*) are the most common foodborne pathogenic bacteria, which can cause serious diseases at very low infectious doses, such as food poisoning, tissue infections, meningitis, septicemia and even death [4,5]. Many methods have been established to detect *E. coli* and *S. aureus*, including standard plate counting method, polymerase chain reaction and immunology-based techniques [6]. Although these methods have their respective advantages, they suffer from various shortcomings such as tedious sample pretreatments, sophisticated instruments and professional operations, which severely limit their extensive applications in clinical diagnosis [7]. Especially, there are relatively few studies on simultaneously detecting multiple bacteria for disease control and public health due to the existence of multiple and mixed infections. Therefore, it is of great importance to exploit novel technologies with short analysis time, easy operation and high sensitivity to realize simultaneous detection of different foodborne pathogenic bacteria.

Over the past couple of years, biosensor, as a new analysis platform, has gained popularity because of its high sensitivity and portability, which combines the advantages of biometric recognition element and physical transducer to achieve a measurable signal [8]. On one hand, biological recognition element has unique superiority in selectively identifying and binding to the target molecules. In general, antibody, aptamer (Apt), antibiotic, and antimicrobial peptide are common recognition elements in biosensor applications. Among them, aptamer receives more concerns because of its low production cost, non-toxicity, high specificity and low sensitivity to temperature [9,10]. Aptamers having high specificity for targets are single strand DNA or RNA molecules, which can be created by an in vitro selection process. At present, all kinds of Apt-based biosensors have been applied for detecting bacteria and even cancer cells. On the other hand, the proper choice of transducer is also extremely important to realize sensitive and specific detection of targets, because the transducer can convert bio-recognition reaction into detectable signals (optical or electrical signals) [11]. Surface-enhanced Raman spectroscopy (SERS) is an analytical technique with molecular fingerprint specificity, which can greatly enhance the Raman signals of molecules adsorbed on or near specific surfaces (such as metallic nanostructures) and even provide the molecular fingerprint of the analytes [12–14]. The aptamer-based (Apt-based) SERS biosensors offer exciting opportunities to achieve selective identification and simultaneous detection of multiple potential pathogens [15].

Theoretically, the high sensitivity of SERS mainly originates from the enhancement of localized electromagnetic field on surfaces of noble metals induced by local surface plasmon resonance (LSPR) [16,17]. Strong surface plasmon coupling, called "hot spots", is typically located in narrow gaps between noble metal nanocrystals and especially at the end of tips of noble metal nanocrystals [18,19]. Plasmonic Au nanostars (NSs) featuring good biocompatibility and multiple sharp branches can produce large amounts of hot spots at the tips and thus exhibit stronger SERS enhancement than Au nanorods or Au nanospheres [20,21]. Based on the above-mentioned reasons, Au NSs have been widely recognized as the most promising SERS biosensing platforms [22,23]. Many researches on SERS detection of mycotoxins by Apt-functionalized Au NSs sensors have been reported. For instance, Huang et al. [24] applied Au NSs@4-MBA@Au nanostructure-based SERS aptasensor and realized SERS detection for Ochratoxin. Li et al. [25] constructed the SERS biosensor based on Au NSs-Ag nanoparticles for detecting AflatoxinB1. However, few studies have

been devoted to SERS detection of pathogen bacteria by Apt-functionalized Au NSs SERS biosensors. In addition, it remains challenging to solve the problem of poor stability and easy aggregation of noble metallic nanoparticles in order to expand their application in SERS detection. It is generally accepted that graphene oxide (GO) has the advantages of large specific surface area, excellent dispersion stability and high biocompatibility, which is acknowledged to be an ideal supporting materials for noble metallic nanoparticles [26–28]. GO not only can inhibit the aggregation of noble metallic nanoparticles, but also capture Raman probe molecules with aromatic structure (e.g. 4-MBA, DTNB) through electrostatic or π-π interactions [29,30]. More importantly, GO can quench the fluorescent background signals of the probe molecules, promote efficient charge-transfer and further improve the sensitivity of SERS detection. As a result, the integration of plasmonic Au NSs and GO will provide a powerful nanoplatform for ultrasensitive SERS detection of bacteria.

Because the concentration of bacteria in real samples is usually extremely low, the pre-concentration of target substance is another effective way to enhance the sensitivity of SERS detection. The design and optimization of magnetic-assisted SERS biosensors based on aptamers recognition is the most commonly used strategy for bacterial detection [31,32]. Fe_3O_4 magnetic nanocrystals have attracted tremendous attention due to their excellent magnetic response, low toxicity and easy preparation, and are often used to capture targets in sample solutions [33,34]. Unfortunately, the bare Fe_3O_4 nanocrystals are easily oxidized in the air and tend to aggregate because of the strong magnetic dipole–dipole interactions between nanocrystals [35]. For improving the stability and dispersibility of Fe_3O_4 nanocrystals, surface modification of Fe_3O_4 nanocrystals by non-magnetic layer (such as SiO_2) is an effective solution [33]. In fact, the coating of Fe_3O_4 nanocrystals with SiO_2 not only can prevent the oxidation and agglomeration of Fe_3O_4 nanocrystals, but can facilitate their biocompatibility since SiO_2 is easily decorated with multiple functional groups such as amino, carboxyl and thiol. Based on the above advantages, the Apt-functionalized $Fe_3O_4@SiO_2$-Au nanocomposites (NCs) have great potential as capture probes, which can not only capture and separate target bacteria from complex solutions by magnet, but also provide abundant aptamer binding sites to form the high-density hot spots [9]. Recently, a novel sandwich-like dual-functional SERS substrate based on indirect detection method has been gaining extensive attention and scientific endorsement [36]. The capture probes/bacteria/SERS tags sandwich nanostructures can achieve the magnetic separation and especially the dual recognition and dual SERS enhancement of target bacteria [37].

Inspired by the above points, we herein proposed an innovative SERS platform based on sandwich assay, which could easily realize the simultaneous detection of *E. coli* and *S. aureus* with high sensitivity and specificity. $Fe_3O_4@SiO_2$-Au NCs were selected as magnetic SERS-active substrate, and the optimum SERS performance was obtained by adjusting the spacing between Au nanocrystals on surfaces of $Fe_3O_4@SiO_2$ nanocrystals. By combining with finite-difference time-domain (FDTD) method, the relationship between interparticle gaps and SERS enhancement behavior was discussed. The optimal Apt-functionalized $Fe_3O_4@SiO_2$-Au NCs were used as capture probes, and their selective capture and enrichment ability for *E. coli* and *S. aureus* were discussed. Meanwhile, the novel SERS tags were designed by co-modifying GO-Au NSs with Raman reporters (DTNB and 4-MBA) with non-overlapping characteristic peaks and aptamers, and the loading density of Au NSs on the surfaces of GO was controlled by adjusting the amount of Au NSs added to the GO dispersion. Based on the electromagnetic field simulation and SERS detection results, the SERS enhancement mechanism of the sandwich assay was proposed and discussed. By optimizing the experimental parameters

including the concentrations of DTNB and 4-MBA during the preparation of SERS tags and the added amount of SERS tags, the sandwich-like capture probes/bacteria/SERS tags structure was built and the SERS platform was used for highly sensitive simultaneous detection of *E. coli* and *S. aureus*. Additionally, our sandwich assay-based SERS platform could also be used for detecting *E. coli* and *S. aureus* in milk samples. Therefore, our study not only further expands the understanding of the enhancement mechanism of the sandwich assay-based SERS platform, but also has great potential for practical applications in ultrasensitive simultaneously detecting multiple foodborne pathogens.

2. Materials and methods

The chemicals, biochemicals and instruments are listed in **Supplementary material**.

2.1. Fabrication of capture probes

Apt-Fe$_3$O$_4$@SiO$_2$-Au NCs capture probes were prepared by combining thiol-modified aptamers with Fe$_3$O$_4$@SiO$_2$-Au NCs, and the detailed preparation procedure of capture probes was illustrated in Scheme 1**A**. Firstly, Fe$_3$O$_4$ nanocrystals were synthesized based on the previously reported method with some improvements [38]. FeCl$_3$·6H$_2$O (1.08 g) was added into EG solution (56 mL) and then stirred for 20 min until fully dissolved, followed by the addition of NH$_4$·Ac (3.08 g), Na$_3$C$_6$H$_5$O$_7$·2H$_2$O (0.32 g) and PEG (0.16 g). After reaction mixture was stirred for 40 min at 50 °C, it was transferred to the 80 mL Teflon-lined autoclave and heated at 200 °C for 8 h. Fe$_3$O$_4$ nanocrystals were finally collected with magnet and rinsed several times. Secondly, a layer of SiO$_2$ was coated on Fe$_3$O$_4$ core by sol–gel method. Fe$_3$O$_4$ nanocrystals (50 mg) were dispersed in ethanol (40 mL) and ultrapure water (10 mL). After the mixed solution was stirred mechanically for 10 min, NH$_3$·H$_2$O solution (1 mL) was added to the dispersion under sonication conditions. TEOS solution (0.2 mL) was added after an hour, and the mixture was further stirred overnight to achieve Fe$_3$O$_4$@SiO$_2$ core–shell nanocrystals. The third step is the preparation of Fe$_3$O$_4$@SiO$_2$-Au NCs. Specifically, the obtained Fe$_3$O$_4$@SiO$_2$ nanocrystals (100 mg) were added in ethanol and sonicated for 20 min. Then, APTES (0.5 mL) acting as the aminating agent was added and stirred for 12 h to form amino-functionalized Fe$_3$O$_4$@SiO$_2$ nanocrystals (Fe$_3$O$_4$@SiO$_2$-NH$_2$ nanocrystals). Meanwhile, Au nanocrystals were synthesized by using the same method as described in our previous work [39]. Subsequently, Au colloid solution (10, 30, 50 and 70 mL) was added into 4 mL of Fe$_3$O$_4$@SiO$_2$-NH$_2$ dispersions, respectively. After sonicating, washing and drying, the Fe$_3$O$_4$@SiO$_2$-Au NCs with different Au contents were obtained, which were named FS-A1, FS-A3, FS-A5 and FS-A7 respectively. Fourthly, the thiolated aptamers specific for *E. coli* (SH-Apt$_1$) and *S. aureus* (SH-Apt$_2$) were activated with TCEP solution, respectively, and then aptamers were combined with
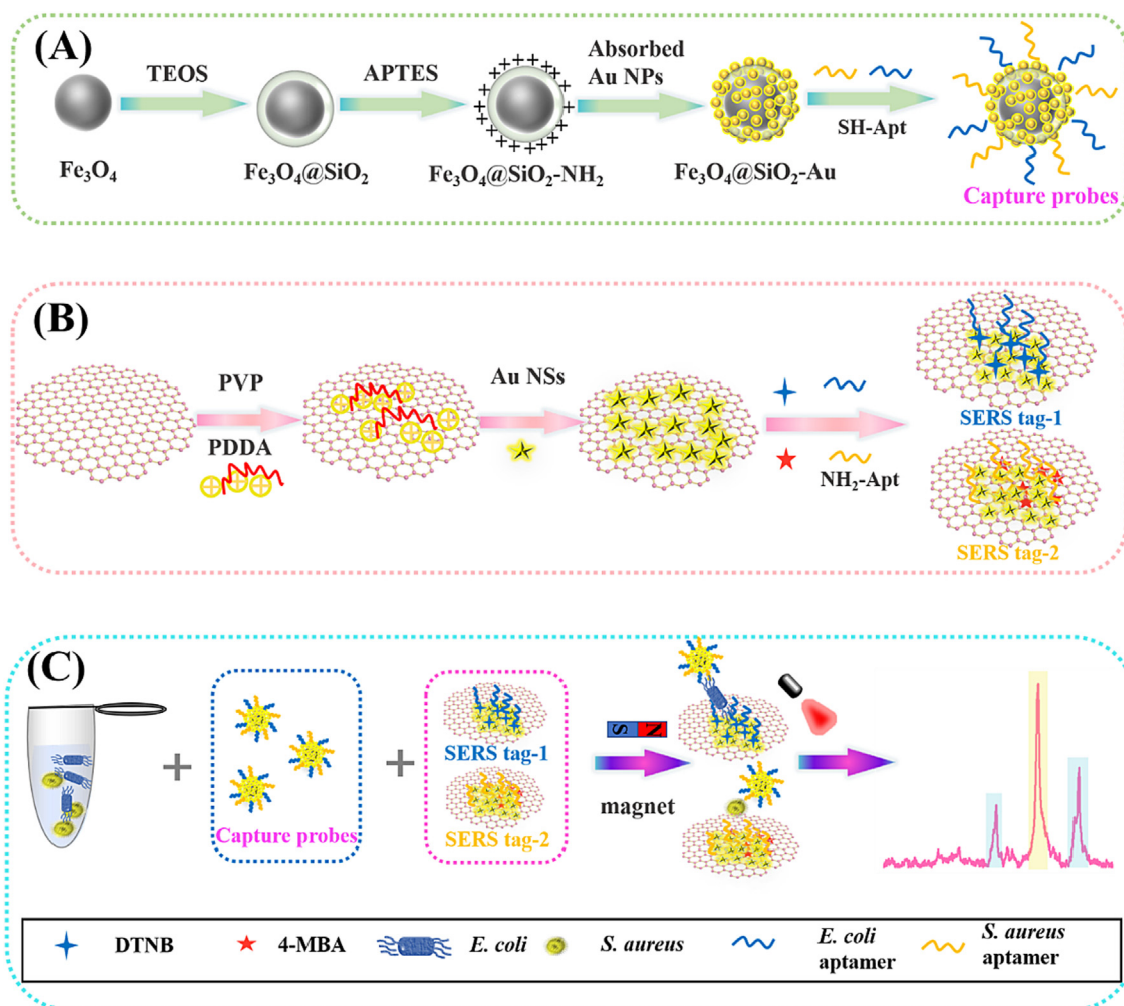
Scheme 1. Schematic diagram of preparation of (A) Apt-Fe$_3$O$_4$@SiO$_2$-Au magnetic capture probes, (B) aptamers conjugated SERS tags and (C) dual-enhanced strategy for simultaneously detecting *E. coli* and *S. aureus*.

$Fe_3O_4@SiO_2$-Au NCs through Au-S bond. Typically, 2 μL of $SH-Apt_1$ and 2 μL of $SH-Apt_2$ were mixed with TCEP solution (1 mM, 2 μL) in dark, respectively. Then, the activated $SH-Apt_1$ and $SH-Apt_2$ were mixed with $Fe_3O_4@SiO_2$-Au NCs dispersions (4 mL, 1 mg/mL). After shaking for 24 h at 37 °C in a thermostatic oscillator, the mixtures were washed with PBS buffer to remove unreacted aptamers, collected with magnet and resuspended in PBS buffer to form capture probes of *E. coli* and *S. aureus*.

2.2. Assembly of SERS tags

SERS tags were obtained by connecting Raman reporter molecules to the synthesized GO-Au NSs, and then combining them with amino-modified aptamers. NH_2-Apt_1 (Apt of *E. coli*) and DTNB were used to synthesize SERS tag-1, while NH_2-Apt_2 (Apt of *S. aureus*) and 4-MBA were used to synthesize SERS tag-2. The synthesis process of SERS tags was shown in Scheme 1**B**. The first step was the preparation of GO, which was based on the modified method described in the literature by Marcano et al. [40]. Briefly, the graphite powder (0.75 g) and $KMnO_4$ (4.5 g) were mixed with concentrated H_2SO_4/H_3PO_4 (9:1, 100 mL), and the prepared mixture was placed into a water bath (preheated to 50 °C). After heating the mixed solution with stirring for 6 h, 30 mL of H_2O_2 solution was added. It could be observed that the color of solution varied from black to bright yellow. The above mixture was further heated and stirred for 3 h, and then cooled and adjusted to pH 6 with ultrapure water. The final dry GO was obtained after centrifuging, washing and drying treatments.

The second step is to modify GO with PVP and PDDA [41]. Concretely, the synthesized GO was dispersed in ultrapure water and ultrasonicated for over 1 h to obtain GO dispersion. PVP (48 mg) was added to GO dispersion (0.5 mg/mL, 12 mL) and the mixture was stirred for 12 h to achieve GO modified with PVP. Subsequently, PVP modified GO was further functionalized by PDDA, and the procedure was as follows. PVP-GO suspension (1 mg/mL, 2 mL) was added to aqueous solution (8 mL) containing KCl (373 mg) and PDDA (1.25 mg/mL, 750 μL), and then the mixture was sonicated for 2.5 h. After product was washed several times by centrifugation, the obtained GO modified with PDDA was stored in the dark for further use.

The third step is the preparation of GO-Au NSs. $HAuCl_4$ solution (0.24 mM, 200 μL) was dropped into ultrapure water (20 mL) under vigorous stirring, and then Au seeds (100 μL), 1 % sodium citrate dihydrate (44 μL), and hydroquinone (30 mM, 2 mL) were added into the above solution one by one, in which sodium citrate dihydrate and hydroquinone were used as reducing agent and morphology inducer, respectively. The above solution was then stirred at room temperature for 30 min to obtain Au NSs, which were dispersed in ultrapure water (5 mL) for further use. Under magnetic stirring, Au NSs (1, 2, 3 and 4 mL) were added to PDDA-GO (160 μL), respectively. The mixture was sonicated for 2 min and then kept overnight. After being collected by centrifugation, the GO-Au NSs with different Au contents were obtained, which were designated by GANS-1, GANS-2, GANS-3 and GANS-4, respectively.

The fourth step is to functionalize GO-Au NSs with DTNB/4-MBA. Typically, DTNB/4-MBA ethanol solution (0.1 mL for each) was added to GO-Au NSs (1 mL) and stirred at 37 °C for 2 h with a speed of 600 rpm. After removing excess DTNB/4-MBA by centrifugation, the products were re-dispersed in MES buffer.

The last step is to activate carboxyl groups on surfaces of DTNB/4-MBA-modified GO-Au NSs. The activated carboxyl groups could bind to amino-modified aptamers. More concretely, EDC (100 mM, 10 μL) and NHS (100 mM, 15 μL) were added into DTNB/4-MBA-modified GO-Au NSs (1 mL) to activate the carboxyl groups [1,42]. After shaking the mixture for 2 h, NH_2-Apt_1/NH_2-

Apt_2 (10 μL) was added and the samples were incubated overnight at 37 °C (240 rpm). Then the products were centrifuged for 10 min at 5000 r/min to remove excess aptamers. For avoiding non-specific adsorption, unreacted carboxyl groups on DTNB/4-MBA-GO-Au NSs were blocked with 1 % BSA under shaking conditions for 2 h. Finally, the prepared SERS tag-1 and SERS tag-2 were respectively resuspended in 1 mL of PBS buffer.

2.3. Optimization of the developed SERS platform

The concentrations of Raman reporter molecules (DTNB, 4-MBA) during the preparation of SERS tags and the added amount of SERS tags were optimized. On one hand, because the SERS signal intensities of *E. coli* and *S. aureus* are closely related to concentrations of DTNB and 4-MBA, it is necessary to optimize the concentrations of DTNB and 4-MBA during the synthesis of two SERS tags. The synthesis conditions of SERS tag-1 and SERS tag-2 were optimized by changing the concentrations of DTNB and 4-MBA (10, 30, 50, 70, 90 and 110 μM). On the other hand, the effect of added amount of SERS tags on SERS signal intensity also needed to be considered. SERS tag-1 and SERS tag-2 were prepared at the optimal concentrations of DTNB and 4-MBA. The optimal addition volume of SERS tags was determined by adding different volumes (20, 40, 60, 80, 100 and 120 μL) of SERS tags to the capture probes/bacteria complexes.

2.4. SERS detection of E. Coli and S. Aureus

The detection of *E. coli* and *S. aureus* was carried out under optimized conditions. *E. coli* (50 μL) and *S. aureus* (50 μL) with different concentrations (10, 10^2, 10^3, 10^4, 10^5, 10^6, 10^7 and 10^8 cfu/mL) were incubated with capture probes at 37 °C for 40 min in a constant temperature shaker, respectively. The capture probes/bacteria complexes were separated by magnet and washed four times with PBS buffer. Then, both SERS tag-1 and SERS tag-2 (10 mg/mL, 100 μL, respectively) were added and incubated at 37 °C for 40 min. After the product was separated by a magnetic field, the sandwich complex was washed with PBS buffer and re-dispersed in 50 μL of PBS buffer. Finally, 50 μL of capture probes/bacteria/SERS tags complexes was dropped on an Al-plate for SERS detection by using a confocal Raman microscope (using 632.8 nm excitation). The concentration of bacteria was decided by measuring the optical density at 600 nm (OD_{600} (*E. coli*) = 1.0 was about 1.0×10^8 cfu/mL, OD_{600} (*S. aureus*) = 1.0 was about 1.5×10^8 cfu/mL).

3. Results and discussion

3.1. Operating principle of novel SERS platform through sandwich immunoassay

The schematic diagram of dual-recognition SERS-based immunoassay platform based on SERS sandwich strategy for the simultaneous detection of *E. coli* and *S. aureus* was shown in Scheme 1**C**. Firstly, $Apt-Fe_3O_4@SiO_2$-Au NCs capture probes were incubated with sample solution containing both *E. coli* and *S. aureus*. The aptamers allowed capture probes to specifically bind to the target bacteria and Fe_3O_4 nanocrystals were conducive to the enhancement of target bacteria. Secondly, both SERS tag-1 and SERS tag-2 were added to the capture probes/bacteria complexes and incubated to form the capture probes/bacteria/SERS tags sandwich nanostructures. SERS tag-1 and SERS tag-2 were formed by connecting two different Raman reporter molecules (DTNB and 4-MBA) and aptamers (NH_2-Apt_1 and NH_2-Apt_2) to GO-Au NSs, respectively, in which the aptamers of *E. coli* and *S. aureus* that

could specifically bind to the target bacteria. After the magnetic sandwich complexes were separated and enriched with magnet, the characteristic SERS spectra (DTNB for *E. coli* and 4-MBA for *S. aureus*) were collected using Raman spectrophotometer. Because the characteristic Raman signal intensity generated by sandwich complexes was proportional to the concentrations of two pathogens, the quantitative analysis of *E. coli* and *S. aureus* could be achieved. Furthermore, due to the introduction of two kinds of aptamers, the simultaneous detection of *E. coli* and *S. aureus* could also be realized. Notably, the combination of capture probes, SERS tags and magnetic enrichment could bring the dual enhancement of SERS signals of target analysts, which will significantly improve the sensitivity of SERS platform based on the sandwich assay.

3.2. Characterazation of Fe₃O₄@SiO₂-Au NCs with different additive amounts of Au nanocrystals

Fe₃O₄@SiO₂-Au NCs composed of Fe₃O₄ core, SiO₂ shell and Au nanocrystals uniformly deposited on Fe₃O₄@SiO₂ nanocrystals were used as SERS active substrate. Morphologies of the samples obtained at each stage of the synthesis procedure were characterized via SEM and TEM images. As depicted in Fig. S1**A(a)** and **S1B (a),** Fe₃O₄ nanocrystals with an average diameter of 270 nm showed regular morphology and good dispersibility. Fig. S1**A(b)** and **S1B(b)** exhibited that Fe₃O₄ nanocrystals were covered uniformly by the amorphous SiO₂ layer (~35 nm in thickness) to form a clear core–shell structure. Subsequently, the surfaces of Fe₃O₄@-SiO₂ nanocrystals were aminated by APTES to make them positively charged, which could adsorb negatively charged citrate-capped Au nanocrystals through the strong affinity between Au

nanocrystals and amine groups [38]. Fig. S1**A(c)** and **S1B(c)** clearly presented that the outermost layer of Fe₃O₄@SiO₂-Au NCs was composed of many tiny Au nanocrystals with a diameter of 13 nm. FT-IR analysis was performed to confirm the changes of their surface functional groups. As illustrated in Fig. S1**C**, Fe₃O₄ nanocrystals exhibited an absorption peak at 587 cm⁻¹, which was attributed to the stretching vibration of Fe-O bond [43]. As for Fe₃O₄@SiO₂ nanocrystals, the characteristic peak of SiO₂ could be seen at 1090 cm⁻¹, indicating that SiO₂ nanocrystals were successfully coated on surfaces of Fe₃O₄ nanocrystals [44]. After functionalizing Fe₃O₄@SiO₂ nanocrystals with APTES, the band appeared at 3430 cm⁻¹ was designated to N—H stretching vibration of –NH₂ group. By contrast, the adsorption band of Si-O bond of Fe₃O₄@SiO₂-Au NCs at 1090 cm⁻¹ decreased dramatically. Given that Au had no absorption in the infrared region, the phenomenon indirectly proved the successful adsorption of Au nanocrystals [44]. EDS results in Fig. S1**D** verified that Fe₃O₄@SiO₂-Au NCs were composed of Fe, O, Si and Au elements. The optical properties of synthesized samples were studied by UV–vis spectroscopy, as shown in Fig. S1**E**. Because Fe₃O₄ nanocrystals were black, no significant absorption peak was observed in a wide wavelength range [45]. Fe₃O₄@SiO₂ nanocrystals had a slightly strong absorption around 400 nm, and the color of solution varied from black to light brown after coating with SiO₂ [38]. Au nanocrystals exhibited a sharp LSPR peak at 520 nm. Differing from Au nanocrystals, Fe₃O₄@SiO₂-Au NCs had an absorption peak around 590 nm wavelength, and especially the range of absorption bond was wider than that of Au colloids. According to Mie's theory, the change in LSPR peak position and broadening of resonance absorption were closely correlated with the extent of aggregation of Au nanocrystals [46].
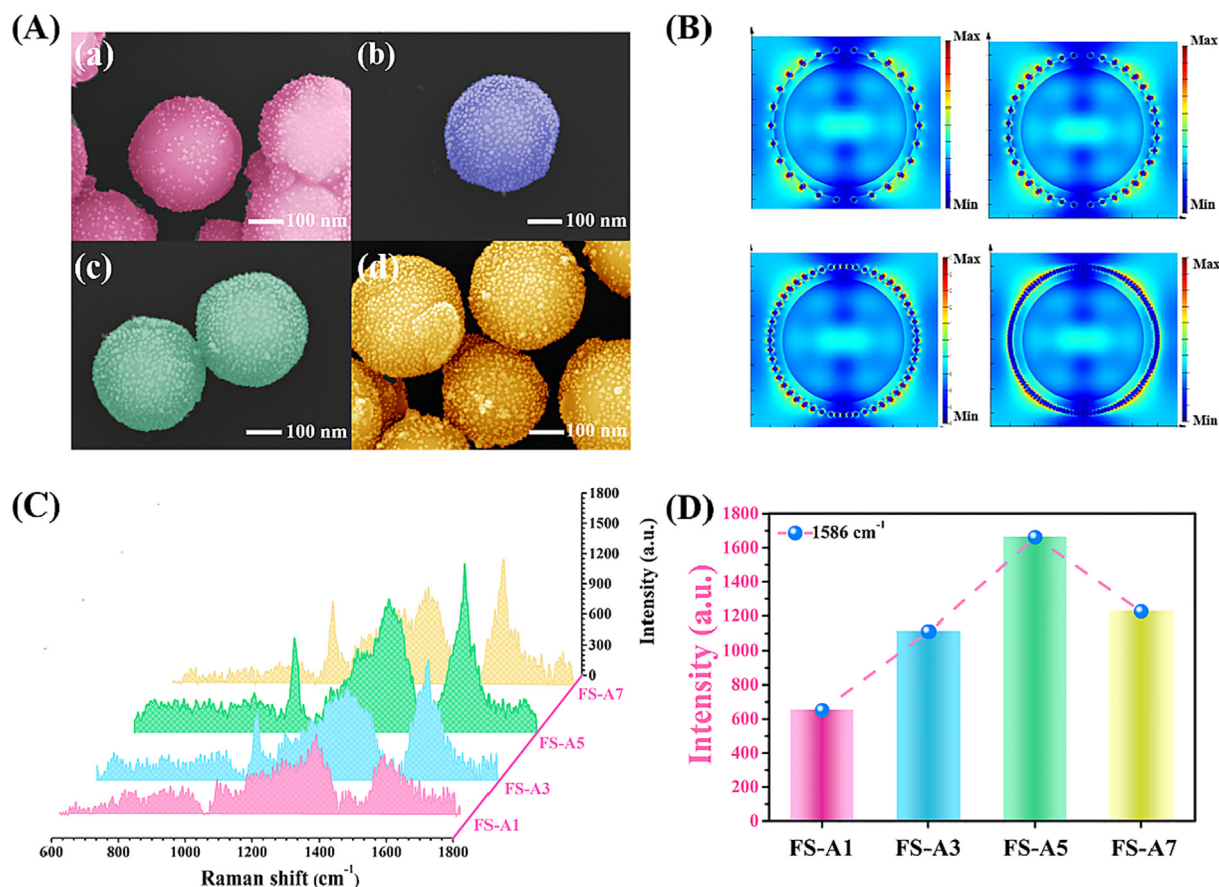

Fig. 1. (A) SEM images and (B) FDTD simulation of (a) FS-A1, (b) FS-A3, (c) FS-A5 and (d) FS-A7, (C) SERS spectra of 4-MBA adsorbed on FS-A1, FS-A3, FS-A5 and FS-A7 and (D) the corresponding SERS intensity comparison at 1586 cm⁻¹.

When Au nanocrystals were attached to the surfaces of Fe_3O_4@-SiO_2-NH_2 nanocrystals, the spaces between Au nanocrystals were shortened, which could lead to red-shift of LSPR peak of Au nanocrystals and broadening of absorption peak. The changes in solution colors of samples were noticed, as presented in the inset of Fig. S1**E**.

Because the nanogap distance in-between adjacent noble metals plays a vital role in the localized electromagnetic field enhancement, Fe_3O_4@SiO_2-Au NCs with different Au interparticle nanogaps were designed and prepared by changing the additive amount of Au colloid solution [47]. Fig. 1**A** presented the SEM images of FS-A1, FS-A3, FS-A5 and FS-A7. It could be found that Au nanocrystals were uniformly deposited on surfaces of Fe_3O_4@SiO_2 for all four Fe_3O_4@SiO_2-Au NCs. The difference was that the nanogap distance between adjacent noble metals was adjusted. Nano measurer software was used for measuring the interparticle spacing of Au nanocrystals on surfaces of Fe_3O_4@SiO_2-Au NCs, and the corresponding histograms of distance between adjacent Au nanocrystals were shown in **Figure S2**. As for FS-A1, FS-A3, FS-A5 and FS-A7, the interparticle spacing of Au nanocrystals was about 50, 30, 20 and 2 nm, respectively. To gain a better understanding of relationship between interparticle gaps and SERS enhancement behavior, the local electric field distribution was simulated by FDTD method depicted in Fig. 1**B**. The simulation results showed that high-intensity local electric field was generated in the nanogaps between Au nanocrystals. In addition, the local electronic field increased when the interparticle gaps of Au nanocrystal reduced from 50 nm to 20 nm. It was reasonable because the interparticle spacing of FS-A5 was smaller than that of FS-A1 and FS-A3, FS-A5 had more hot spots. But when the nanogaps were further reduced, the local electric field decreased abnormally. This might be explained by a reduction of plasmonic coupling effect [48]. The excess Au nanocrystals on the surfaces of Fe_3O_4@SiO_2 could easily lead to agglomeration of Au nanocrystals and even formation of Au shells, thus reducing the number of hot spots. In order to provide experimental evidence to verify the FDTD simulation results, 4-MBA was selected as Raman reporter molecule to evaluate the SERS performance of Fe_3O_4@SiO_2-Au NCs. SERS spectra of 4-MBA adsorbed on FS-A1, FS-A3, FS-A5 and FS-A7 and the corresponding SERS intensity comparison at 1586 cm^{-1} were illustrated in Fig. 1**C and 1D**. When increasing the additive amount of Au colloid solution, the SERS intensity of 4-MBA increased first and then decreased, which was consistent with FDTD simulation. FS-A5 exhibited optimal performance as SERS substrate for detecting 4-MBA, which was chosen as the following magnetic SERS substrate.

3.3. Characterization of Apt-conjugated FS-A5 capture probes

The thiol-modified aptamers were combined with FS-A5 through Au-S bond, and the assembly process of the magnetic capture probes Apt-FS-A5 was monitored by UV–vis spectroscopy, zeta potential, and FI-IR measurements. As presented in Fig. 2**A**, aptamers had a typical absorption peak at 260 nm, which was ascribed to the absorption of nucleic acid bases. The absorbance at 260 nm was also found in Apt-FS-A5, which indirectly confirmed the successful binding of FS-A5 to aptamers. Moreover, it could be observed from enlarged view of Fig. 2**A** that the absorption peak of magnetic capture probes Apt-FS-A5 had a significant red shift relative to that of FS-A5, further indicating that the aptamers interacted with FS-A5 through Au-S bond [49]. The changes of the zeta potential before and after aptamers modification also can be used to determine the binding of aptamers on FS-A5. As depicted in Fig. 2**B**, zeta potential of Fe_3O_4@SiO_2-NH_2 nanocrystals was measured as positive owing to the presence of positive-charged amino groups, suggesting the successful functionalization of $-NH_2$ groups on surfaces of Fe_3O_4@SiO_2 nanocrystals. The further assembly of

negative-charged citrate-modified Au nanocrystals on surfaces of Fe_3O_4@SiO_2-NH_2 nanocrystals caused the zeta potential of FS-A5 to become negative [38]. After incubation of aptamer with FS-A5, the zeta potential value of Apt-FS-A5 was further decreased because the aptamers at neutral pH carried a negative charge [50]. Furthermore, FT-IR analysis in Fig. 2**C** was also performed to affirm the successful preparation of Apt-FS-A5. Compared with unmodified FS-A5, the new peaks at 960 cm^{-1} and 1640 cm^{-1} appeared in FT-IR spectrum of Apt-FS-A5, which were assigned to symmetrical stretching vibration of phosphates in nucleoside and the stretching vibration and bending vibration of P—O, respectively [51]. The effect of aptamers modification on the magnetic properties of FS-A5 was also studied. Fig. 2**D** showed the hysteresis loops of the prepared Fe_3O_4, FS-A5 and Apt-FS-A5. It could be seen that all the samples showed superparamagnetic characteristics, and the saturation magnetization (Ms) values of Fe_3O_4, FS-A5 and Apt-FS-A5 were 40.95, 15.86 and 14.35 emu/g, respectively. Compared with bare Fe_3O_4 nanocrystals, the Ms value of FS-A5 decreased due to the mass effect and diamagnetic shielding of SiO_2 and Au nanocrystals. However, FS-A5 could still be completely collected by a magnet from the mixture within 20 s, as depicted in the inset of Fig. 2**D**. It was worth noting that the aptamers coating had almost no effect on the magnetic properties of FS-A5. Therefore, Apt-FS-A5 could be qualified to separate the target molecules from mixed solution with the help of magnet.

3.4. Capture ability of Apt-FS-A5 to E. Coli and S. Aureus

The selective recognition capability and the capture ability of the aptamers to targeted bacteria are closely correlated with the capture efficiency of Apt-based biosensors. The ability of Apt-Fe_3O_4@SiO_2-Au NCs (capture probes) to capture *E. coli* and *S. aureus* was evaluated. **Figure S3** showed the SEM images of the original *E. coli* and *S. aureus*. After Apt-Fe_3O_4@SiO_2-Au NCs (Apt-FS-A5) were incubated with *E. coli* and *S. aureus*, respectively, capture probes/*E. coli* and capture probes/*S. aureus* complexes were separated magnetically. Fig. S4**A(a)** and **S4(b)** showed that *E. coli* or *S. aureus* could be captured successfully by capture probes from complex solutions. The traditional plate counting method was further adopted to investigate the capture ability of Apt-Fe_3O_4@SiO_2-Au NCs to target bacteria [1]. Apt-Fe_3O_4@SiO_2-Au NCs (Apt-FS-A5) were added to 200 μL of bacterial suspensions ($\sim10^4$ cfu/mL for *E. coli* and *S. aureus*), respectively. After incubating for 20 min, Apt-Fe_3O_4@SiO_2-Au/bacteria complexes were separated with help of magnet. Subsequently, 100 μL of the supernatant from each group was streaked on Luria-Bertani (LB) agar and incubated overnight. For purpose of comparison, the same experimental procedure was performed on blank and non-modified capture probes. As illustrated in Fig. S4**B**, the photographs of plate agar plate indicated that most of bacteria were captured by Apt-FS-A5 in contrast to blank and non-modified FS-A5. The capture efficiency was achieved by counting the remaining bacteria [7]. Results in Fig. S4**C** suggested that capture efficiency of capture probes for *E. coli* and *S. aureus* was as high as 80 % and 76 %, respectively, which was higher than the previous reports [52,53]. On the basis of these results, it was obvious that the well-designed capture probes could specifically bind and efficiently capture the target bacteria from the complex solutions.

3.5. Characerazation and optimization of GO-Au NSs

The combination of GO and Au NSs was used as a strategy to design SERS tags, which integrated the advantages of excellent enrichment ability of GO and high SERS activity of Au NSs [41]. Microscopic morphologies of the as-prepared GO, Au NSs and GO-Au NSs were characterized by TEM. As presented in Fig. S5**A**
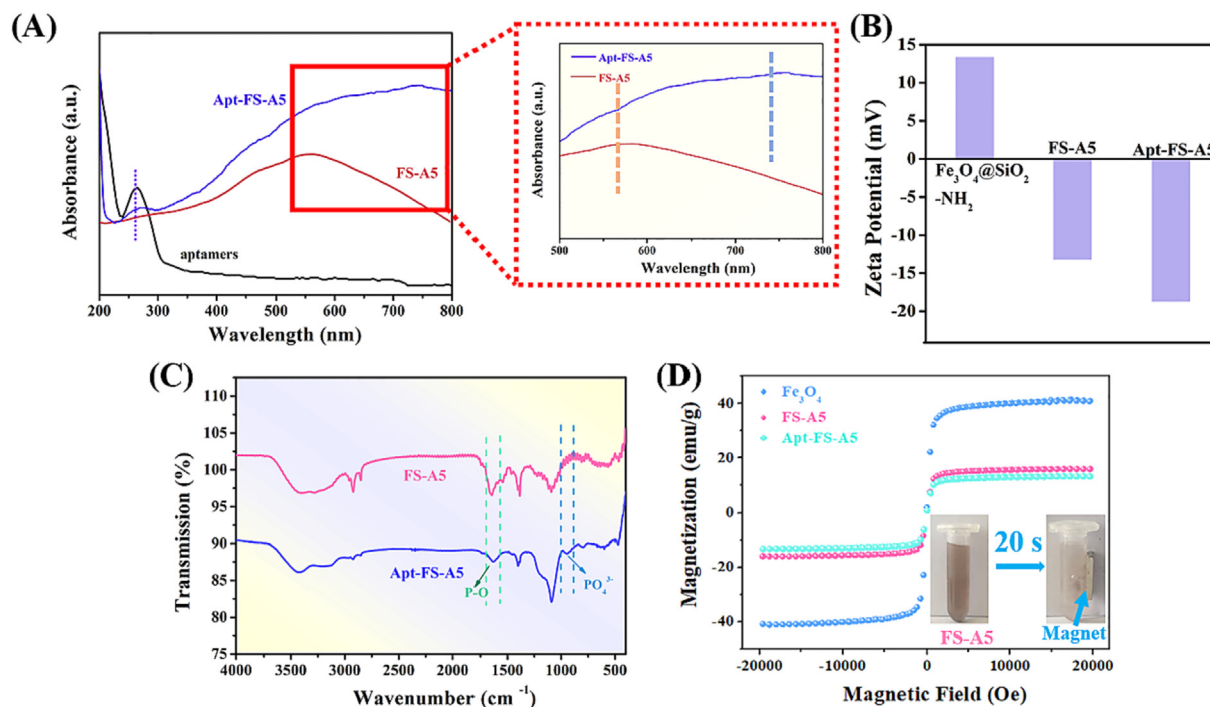
Fig. 2. (A) UV–vis spectra of aptamers, FS-A5 and Apt-FS-A5 (the red box was the corresponding enlarged view), (B) zeta potential values of Fe₃O₄@SiO₂-NH₂, FS-A5 and Apt-FS-A5, (C) FT-IR spectra of FS-A5 and Apt-FS-A5 and (D) hysteresis loops of Fe₃O₄, FS-A5 and Apt-FS-A5. The inset of (D) was the photograph of FS-A5 before and after separation by magnet.

(a), GO exhibited the translucent layered structure with various degrees of wrinkles. Fig. S5**A(b)** clearly showed that Au NSs were composed of central core and multiple sharp and irregular branches. As for GO-Au NSs, it could be seen from Fig. S5**A(c)** that Au NSs were deposited on the surfaces of GO. Meanwhile, the wrinkles of GO could be clearly observed around Au NSs, which could provide abundant active sites for the adsorption of Au NSs. The successful preparation of GO-Au NSs was also indirectly confirmed by the presence of C, O, Au elements in EDS analysis (Fig. S5**B**). The sequential modification and self-assembly process of GO-Au NSs were further understood by measuring the zeta potentials of GO, GO-PVP, GO-PDDA, Au NSs and GO-Au NSs reflected in Fig. S5**C**. The abundant negatively charged carboxyl and hydroxyl groups on the surfaces of GO let it carry negative charges, and the introduction of amphiphilic PVP molecules made the surface charge of GO more negative, which could be proved by the change in zeta potential from −30.3 mV for GO to −36.1 mV for GO-PVP [41]. Once the surfaces of GO-PVP were functionalized with positively charged PDDA through electrostatic attraction, the crossover in zeta potential from negative to positive value (+34.3 mV) was observed. After the negatively charged Au NSs (-31.3 mV) were further immobilized onto the surfaces of positively charged GO-PDDA, zeta potential value of the resulting GO-Au NSs was measured to be + 13.9 mV. Fig. S5**D** showed the XRD patterns of GO and GO-Au NSs. The XRD spectrum of GO presented a sharp diffraction peak in the small angular region (2θ = 11.02°), corresponding to the d-spacing of 8.86 Å for (0 0 1) plane [54]. After loading Au NSs on GO, four new peaks appeared at 38.24°, 44.47°, 64.85° and 77.86°, which were assigned to (1 1 1), (2 0 0), (2 2 0) and (3 1 1) planes of Au (face-centered-cubic structure, JCPDS No. 04–0748), implying the successful preparation of GO-Au NSs [26]. **Figure S6** exhibited the UV–vis spectra of GO-PDDA, Au NSs and GO-Au NSs. The characteristic absorption peak of GO at 230 nm was attributed to π–π* electronic transition of C=C band, which could also be observed in both GO-PDDA and GO-Au

NSs [55]. Au NSs presented a very broad LSPR band between 500 and 800 nm with the strongest absorption peak at 675 nm, and the expansion of LSPR bandwidth might be attributed to the difference in length and sharpness of branches of Au NSs [23]. Moreover, the UV–vis absorption spectrum of GO-Au NSs had a blue shift of LSPR wavelength compared with that of Au NSs, which might be caused by the electronic interaction between GO and Au NSs and the change in dielectric constant.

It is generally known that the property of SERS substrate depends strongly upon size, shape, density of noble metal nanocrystals and especially the number of hot spots [56]. By adjusting the addition amounts of Au NSs in GO-PDDA dispersion, the loading amounts of Au NSs on GO-Au NSs could be effectively controlled and thus the SERS performance of GO-Au NSs could be regulated. As shown in the TEM images of Fig. 3**A(a-d)**, the number of Au NSs loaded on the surfaces of GO increased with the increase of amount of Au NSs in the reaction system. At first, Au NSs loaded on the surfaces of GO distributed sporadically. Then, the distribution of Au NSs became dense until the Au NSs agglomerated in the end. The corresponding UV–vis spectra of GANS-1, GANS-2, GANS-3 and GANS-4 depicted in Fig. 3**B** presented that the relative intensity of absorption peak at ∼ 675 nm increased, verifying the increased loading amount of Au NSs on surfaces of GO, which was consistent with the above results of TEM analysis [26]. It could also observed from Fig. 3**B** that the LSPR bands exhibited a slight red shift when increasing the addition amounts of Au NSs, which might be due to the increased plasmon coupling caused by the decreasing distance between Au NSs on surfaces of GO [57]. Furthermore, to evaluate the SERS enhancement ability of GO-Au NSs with various Au NSs amounts, different Raman molecules including DTNB and 4-MBA were used to perform SERS measurements. As presented in Fig. 3**C and 3D**, Raman characteristic peaks of DTNB and 4-MBA were detected easily for all the SERS substrates [58]. The peak at 1337 cm⁻¹ for DTNB and 1586 cm⁻¹ for 4-MBA were chosen for comparison of SERS peak intensity (Fig. 3**E)**. It
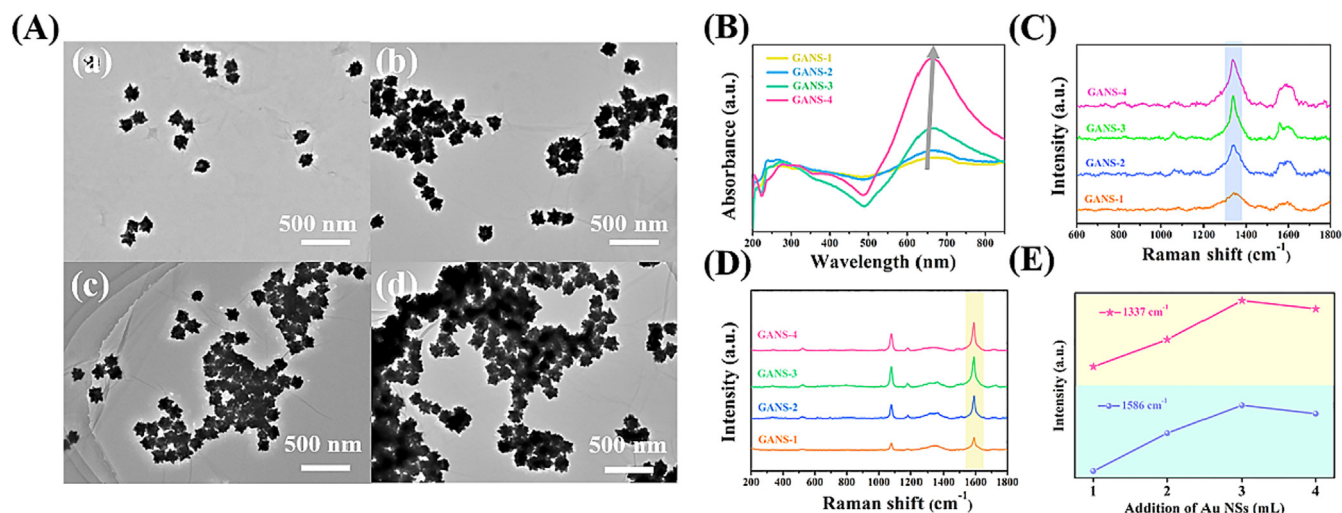
Fig. 3. (A) TEM images of (a) GANS-1, (b) GANS-2, (c) GANS-3 and (d) GANS-4, (B) UV–vis absorption spectra of GANS-1, GANS-2, GANS-3 and GANS-4, SERS spectra of (C) DTNB and (D) 4-MBA adsorbed on GO-Au NSs with different additive amounts of Au NSs and (E) the corresponding SERS peak intensity at 1337 cm^{-1} and 1586 cm^{-1}, respectively.
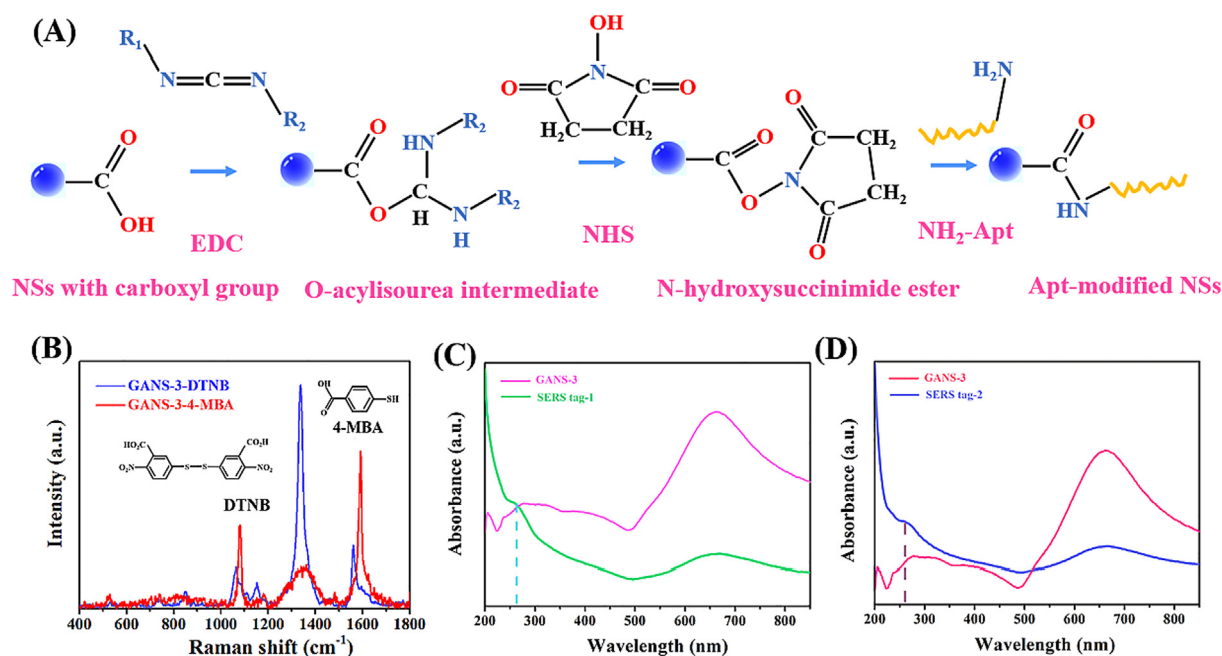

Fig. 4. (A) Schematic diagram of EDC/NHS-activated carboxyl group for attachment with amino-modified aptamer, (B) molecular structure of Raman reporter molecules (DTNB, 4-MBA) and SERS spectra of GANS-3-DTNB and GANS-3–4-MBA, UV–vis absorption spectra of (C) SERS tag-1 and (D) SERS tag-2.

could be obviously observed that the maximum values of the peak intensity for both DTNB and 4-MBA appeared when GANS-3 was acted as SERS substrate. This phenomenon could be explained by the following reasons. When increasing the addition amount of Au NSs, more hot spots were produced between Au NSs dispersed on the surfaces of GO, which could enhance the SERS signals of target molecules [59]. However, the further increase of the additive amount of Au NSs inevitably led to the aggregation of Au NSs, as verified by TEM results, and thus reduced the number of hot spots, which was unfavorable to the enhancement of SERS signals.

3.6. Characterization of SERS tags

A representative SERS tag generally consists of three basic components: plasmonic nanoparticles as SERS-enhanced substrate,

Raman reporter molecules connected to SERS substrate that could generate characteristic SERS signals, and aptamer for the specific recognition of target molecules [60]. In this study, GANS-3 with the best SERS performance was selected as the SERS active substrate to prepare SERS tags. DTNB and 4-MBA, two common aromatic compounds containing sulfhydryl and negatively charged carboxyl functional groups, were chosen as Raman active reporter molecules, which could be easily captured by GANS-3 through the Au-S bond, electrostatic and π-π interactions. The coupling of aptamer was carried out by the commonly used EDC/NHS cross-linking reaction. Specifically, the surfaces of DTNB/4-MBA-modified GO-Au NSs (GANS-3-DTNB or GANS-3–4-MBA) were modified by EDC-NHS to activate carboxyl groups, and then further functionalized with amino-modified aptamer (NH$_2$-Apt$_1$ or NH$_2$-Apt$_2$) [61]. The specific schematic reaction was depicted in Fig. 4**A**. In the acti-
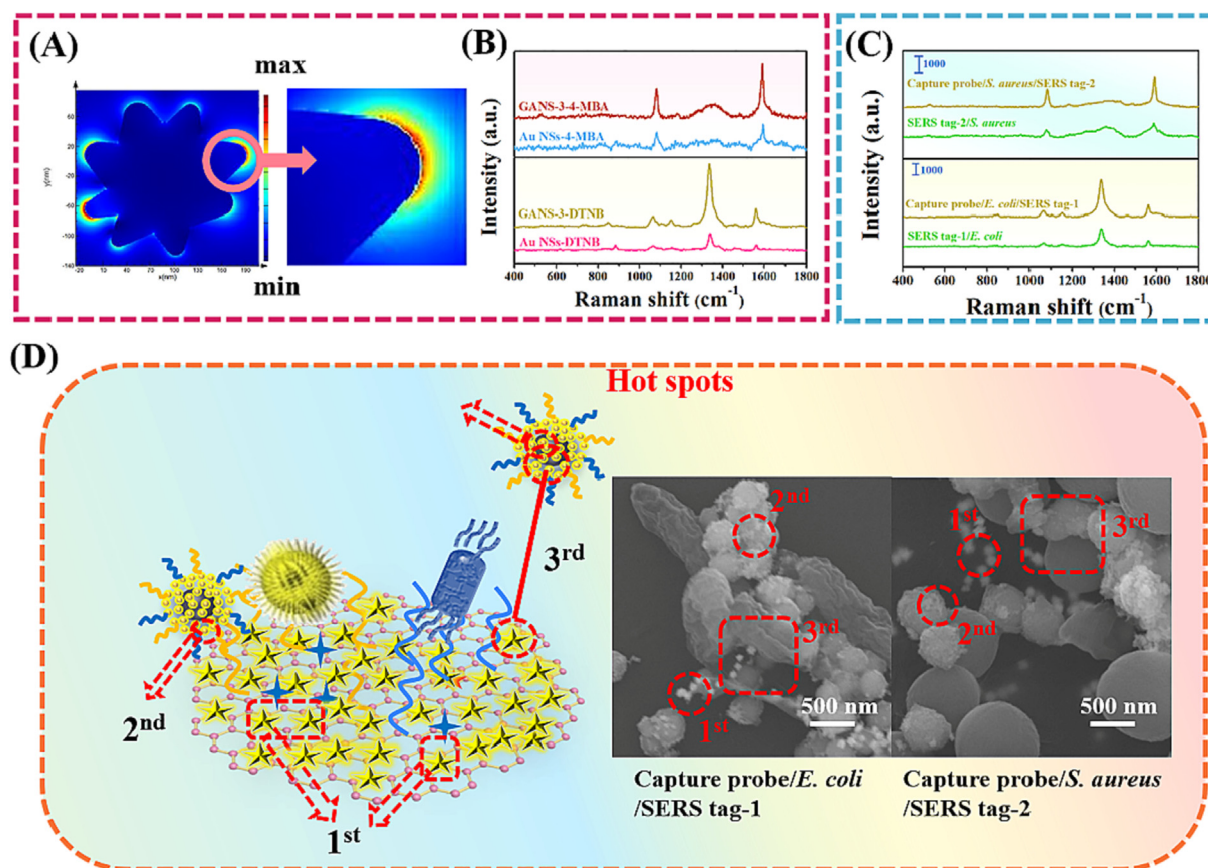
Fig. 5. (A) Electric field distributions of a single Au NS, (B) SERS spectra of DTNB or 4-MBA adsorbed on Au NSs and GANS-3, (C) SERS spectra of SERS tag-1/*E. coli*, capture probe/*E. coli*/SERS tag-1 incubated with *E. coli* and SERS spectra of SERS tag-2/*S. aureus*, capture probe/*S. aureus*/SERS tag-2 incubated with *S. aureus*, (D) SEM images of the sandwich-structured capture probe/bacteria/SERS tags NCs and the corresponding schematic of spatial distribution of SERS hot spots.

vation process of EDC/NHS, the double bond of carbodiimide reagent was attacked by carboxyl groups to form an O-acylisourea intermediate that could react with the amino groups [62]. Because the intermediate was unstable in aqueous solution, the presence of NHS reactants could convert the intermediate into a more stable *N*-hydroxysuccinimide ester to eventually form covalent amide bonds by crosslinking with the amino-modified aptamer [63,64]. SERS spectra of DTNB and 4-MBA absorbed on GANS-3 SERS substrate were shown in Fig. 4**B**. Two non-overlapping characteristic peaks at 1337 cm^{-1} for DTNB and 1586 cm^{-1} for 4-MBA were selected for the following quantitative detection of *E. coli* and *S. aureus*, respectively. The covalent attachment of the aptamers to GANS-3-DTNB and GANS-3–4-MBA could be characterized by UV–vis spectroscopy. The conjugation of aptamers was verified by the peak at 260 nm that referred to the absorption of nucleic acid bases displayed in Fig. 4**C and 4D**, which indirectly suggested the successful preparation of SERS tag-1 and SERS tag-2.

3.7. SERS detection mechanism of sandwich assay

As mentioned above, the anisotropic Au NSs with multiple sharp branches had stronger SERS enhancement than spherical or rod-like nanostructures because there were lots of hot spots at the tips of Au NSs. The electromagnetic field distribution of a single Au NS was simulated using FDTD method. As exhibited in Fig. 5**A**, it was obvious that the highly localized electric field enhancement was located at the tips of Au NSs. Besides constructing lots of high-density hot spots at the tips of Au NSs and in the narrow gaps between Au NSs, the efficient adsorption of target molecules on/

nearby the hot spots regions was another valid way to further improve the sensitivity of SERS detection [65,66]. GO with high specific surface area could enrich more target molecules through electrostatic and π-π interactions [67,68]. In order to determine the role of GO, DTNB and 4-MBA were selected as probe molecules to compare the SERS performance of GO-Au NSs (GANS-3) and bare Au NSs, respectively, as shown in Fig. 5**B**. When DTNB or 4-MBA was conjugated with bare Au NSs, the obvious SERS signals were observed. In comparison, in the presence of GO, GANS-3 exhibited a higher SERS enhancement. This result was reasonable because GO could provide additional chemical enhancement contribution to SERS signals through charge transfer between GO and the target molecules [69,70]. In addition, the SERS performance of SERS tag/bacteria and sandwich-structured magnetic capture probe/bacteria/SERS tag NCs was compared. Fig. 5**C** showed the SERS spectra of the SERS tag/bacteria and the sandwich-like capture probe/bacteria/SERS tag incubated with target bacteria. As could be seen that the intensity of SERS signal of target molecules absorbed on the sandwich-like SERS substrates was much higher than that absorbed on the SERS tag/bacteria. Structurally, unlike the SERS tag/bacteria, sandwich-structured capture probe/bacteria/SERS tag NCs could realize the dual SERS enhancement of target bacteria (*E. coli* or *S. aureus*) because both capture probe and SERS tag could be immobilized on the surfaces of the corresponding bacteria due to the specific recognition ability of the aptamers, as proved by SEM images in Fig. 5**D**. From the point of view of mechanism, the significant enhancement of the sandwich-like capture probe/bacteria/SERS tags could mainly be attributed to the following three factors: (i) the high SERS performance of SERS tags, which was ascribed to the tip hot spots effect of Au NSs, the LSPR effect in

the narrow nanogaps between adjacent Au NSs assembled on surfaces of GO and chemical enhancement contribution through charge transfer between GO and the target molecules (1st hot spots); (ii) the LSPR effect between Au nanocrystals on the surfaces of capture probes (2nd hot spots); (iii) dual signal enhancement resulting from the plasmon coupling of the capture probes and the SERS tags (3rd hot spots) [71]. Moreover, because SERS tags had the large specific surface area, surface binding sites and flexible membrane fluidity and the magnet-assisted enrichment of sandwich-like SERS substrates could lead to increase hot spots density per unit volume, the use of laser can better irradiate the bacterial surface to enhance the SERS signals to a certain extent.

3.8. Optimization of the SERS platform based on sandwich assay

The SERS platform for ultrasensitive detecting target bacteria was attributed to the formation of "capture probes/bacteria/SERS tags" sandwich nanostructures. The key feature of this kind of sandwich assay was to replace the SERS signals of target bacteria with the SERS signals of reporter molecules, which belonged to the indirect detection of target bacteria. Therefore, in order to achieve the optimal SERS platform based on sandwich assay for *E. coli* and *S. aureus* detection, the concentrations of molecules (DTNB and 4-MBA) and the amount of SERS tags (SERS tag-1 and SERS tag-2) were optimized. Results in **Figure S7** showed that 90 μM for DTNB and 70 μM for 4-MBA should be chosen as the optimum concentrations in the preparation process of SERS tag-1 and SERS tag-2, respectively. The optimal amount of SERS tag-1

for *E. coli* and SERS tag-2 for *S. aureus* was 80 μL and 100 μL, respectively.

3.9. Sensitive and specific SERS detection of E. Coli and S. Aureus

Under optimal conditions, sandwich assay-based SERS platform with high sensitivity and exceptionally specificity was used for simultaneously detecting *E. coli* and *S. aureus*. In order to improve the repeatability of SERS signals, the Raman spectrometer was used to randomly measure 5 spots on the "capture probes/bacteria/SERS tags" sandwich structures. The SERS spectral data obtained were averaged to generate repeatable SERS signals. Fig. 6**A** presented the average SERS spectra of "capture probes/bacteria/SERS tags" sandwich structures incubated with different concentrations ($10–10^8$ cfu/mL) of *E. coli* and *S. aureus*. The SERS spectrum of the PBS solution without any bacteria served as a blank control was also exhibited in Fig. 6**A**. It could be observed that when the concentration of *E. coli* and *S. aureus* increased from 10 to 10^8 cfu/mL, the intensities of SERS signals gradually increased. Meanwhile, it can be found that even if the bacterial concentration drops to 10 cfu/mL, the SERS peak intensity is stronger than that of the blank control. What is more, the high-sensitivity simultaneous detection of *E. coli* and *S. aureus* could be easily achieved. The peaks of SERS spectra at 1337 cm^{-1} and 1586 cm^{-1} were used for quantitative analysis of *E. coli* and *S. aureus*, respectively. A strong linear correlation between the SERS intensity and logarithm of the concentration of *E. coli* (y = 815.83 x + 643.04, R^2 = 0.994) and *S. aureus* (y = 354.94 x + 908.97,
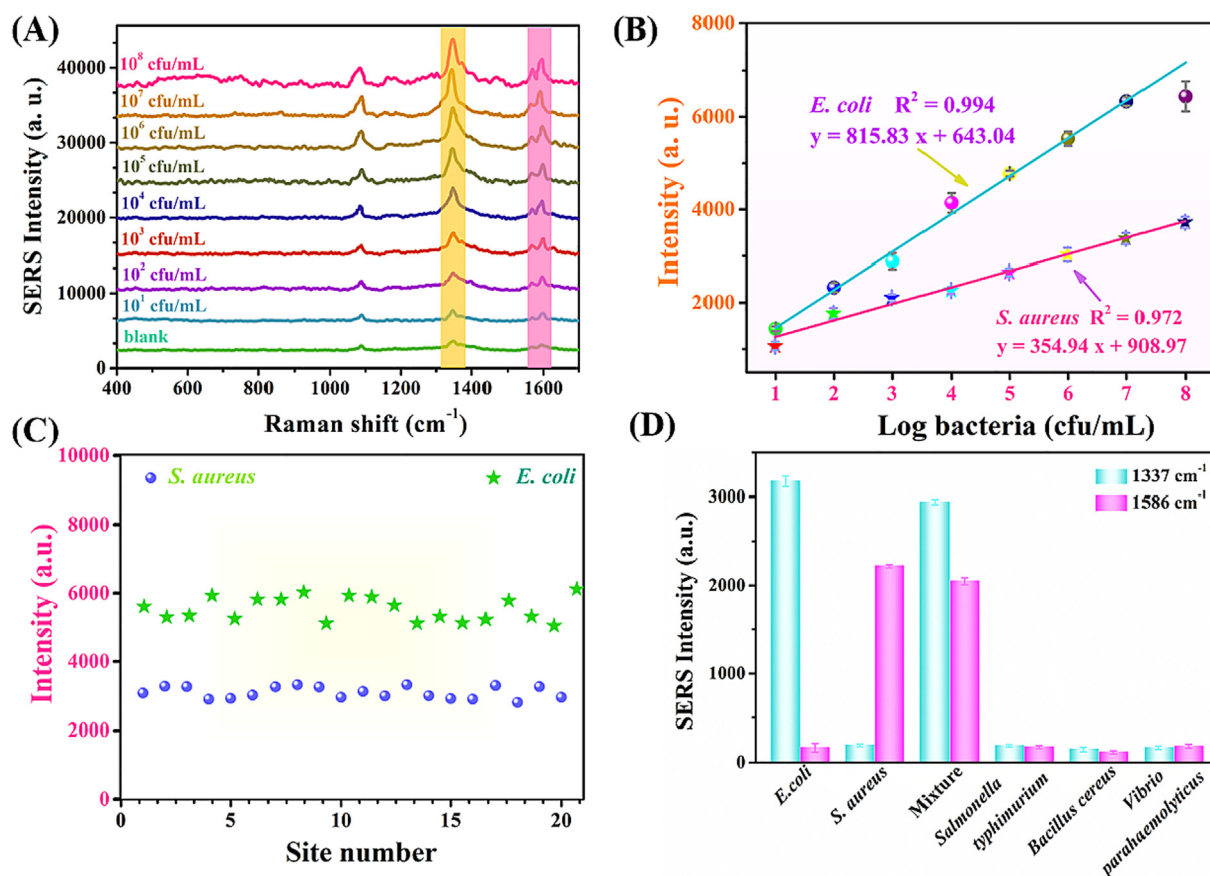

Fig. 6. (A) Average SERS spectra of the "capture probes/bacteria/SERS tags" sandwich structures incubated with different concentrations of *E. coli* and *S. aureus*, (B) linear correlation between logarithms of bacteria concentrations and SERS intensities: peak at 1337 cm^{-1} for *E. coli* and 1586 cm^{-1} for *S. aureus*, (C) SERS intensities of the peaks at 1337 cm^{-1} and 1586 cm^{-1} collected from 20 random spots on SERS substrates, (D) SERS signal intensities at 1337 and 1586 cm^{-1} of as-proposed SERS platform incubated with *E. coli*, *S. aureus*, the mixture of *E. coli* and *S. aureus*, *Salmonella typhimurium*, *Bacillus cereus*, and *Vibrio parahaemolyticus*.

Table 1

Comparison of various SERS substrates and biorecognition agents for detection of bacteria.

SERS substrates (capture probes/SERS tags)	Biorecognition agents	Bacteria	LOD (cfu/mL)	Reference
MSNs/AuNR Ag NFs@SiO$_2$	aptamers	*S. aureus*	17	[72]
Fe$_3$O$_4$@Au MNPs/Au	vancomycin, aptamers	*E. coli* and *S. aureus*	20 and 50	[7]
MBs/PLL coated triple-bond coded Au NPs	antibodies	*E. coli* and *S. aureus*	10 and 25	[73]
AuNPs-PDMS film/Au@Ag NFs	aptamers	*S. aureus*	13	[74]
Fe$_3$O$_4$@SiO$_2$-Au/GO-Au NSs	aptamers	*E. coli* and *S. aureus*	10 and 10	this work

$R^2 = 0.972$) could be observed (Fig. 6**B**) [48]. It could be concluded that the proposed SERS platform had low LOD value of 10 cfu/mL for both *E. coli* and *S. aureus*. Compared with other SERS substrates and biorecognition agents for detecting bacteria, as displayed in Table 1, the as-proposed SERS platform exhibited high SERS sensitively. Furthermore, the reproducibility and stability of SERS signal based on the SERS platform was evaluated by randomly selecting 20 points from the mixed suspension of *E. coli* and *S. aureus* with the concentration of 10^6 cfu/mL. As revealed in Fig. 6**C**, the SERS intensity distributions at both 1337 cm^{-1} and 1586 cm^{-1} were highly uniform and the relative standard deviation (RSD) values were 6.41 % and 5.64 %. In order to study the specific recognition of the as-proposed SERS platform, several common foodborne pathogenic bacteria including *Salmonella typhimurium*, *Bacillus cereus*, and *Vibrio parahaemolyticus* were chosen as interfering bacteria. The concentrations of both *E. coli* and *S. aureus* were set to be 10^3 cfu/mL, whereas the concentrations of all interfering bacteria groups were set to be 10^7 cfu/mL. The mixture included *E. coli* and *S. aureus* (10^3 cfu/mL for each). As illustrated in Fig. 6**D**, there were no obvious SERS signals at both 1337 cm^{-1} and 1586 cm^{-1} when as-proposed SERS platform was incubated with the interfering bacteria. However, once the SERS platform was incubated with *E. coli*, *S. aureus* or the mixture of *E. coli* and *S. aureus*, SERS signals at 1337 and 1586 cm^{-1} could be clearly identified.

3.10. Simultaneous detection of E. Coli and S. Aureus in food samples for practical use of sandwich assay-based SESR platform

In order to evaluate the practical applicability, our proposed sandwich assay-based SERS platform was used to detect milk samples spiked with different concentrations (10^2, 10^3 and 10^4 cfu/mL) of the mixed suspension of *E. coli* and *S. aureus* according to the protocol described above. SERS spectra of "capture probes/bacteria/SERS tags" sandwich structures incubated with milk samples containing various concentrations of *E. coli* and *S. aureus* depicted in **Figure S8** were almost the same as those incubated with PBS solution (Fig. 6**A**), indicating that the presence of complex components in milk samples did not interfere with bacterial detection. SERS peak intensities at 1337 cm^{-1} and 1586 cm^{-1} with different concentrations of *E. coli* and *S. aureus* were used for calculating the amounts of the two target bacteria according to the calibration curves in Fig. 6**B**. **Table S1** summarized the analytical results of the three milk samples. The recovery rates for *E. coli* and *S. aureus* were ranged from 92.8 % to 111.1 % and 91.2 % to 104.9 %, and the RSD values ranged from 4.3 % to 5.0 % and 3.5 % to 6.9 %, respectively. Thus, the obtained results demonstrated that the proposed SERS platform had high stability and good repeatability for simultaneously and quantitatively detecting *E. coli* and *S. aureus* in food samples.

4. Conclusions

In conclusion, a high-performance SERS platform based on sandwich assay for ultrasensitive simultaneous detection of *E. coli* and *S. aureus* has been successfully developed. Apt-functionalized Fe$_3$O$_4$@SiO$_2$-Au NCs were used as capture probes

for capturing and separating bacteria, and GO-Au NSs connected with two kinds of Raman reporter molecules (DTNB and 4-MBA) and aptamers were acted as SERS tags, in which the SERS intensities of DTNB at 1331 cm^{-1} and 4-MBA at 1586 cm^{-1} were utilized for quantitative analysis of *E. coli* and *S. aureus*, respectively. FDTD simulations indicated that the plasma coupling and hot spots distribution of Au nanocrystals on the surfaces of Fe$_3$O$_4$@SiO$_2$ nanocrystals could be adjusted by changing the addition amount of Au colloid solution. Similarly, the optimization of SERS tags could also be achieved by tuning the loading amount of Au NSs on GO. In the presence of *E. coli* and *S. aureus*, a sandwich-like structure, "capture probes/bacteria/SERS tags", was constructed by the specific interaction between aptamer and target bacteria. Under optimal conditions, when concentrations of *E. coli* and *S. aureus* ranged from 10^1-10^8 cfu/mL, the SERS signal intensity and the logarithm of concentration of *E. coli* and *S. aureus* showed a strong linear correlation, and the LOD for simultaneously detecting *E. coli* and *S. aureus* was as low as 10 cfu/mL. Our sandwich assay-based dual-enhanced SERS platform exhibits lower LOD values compared with the previously reported SERS biosensors, which may benefit from the following four points: (i) hot spots effect at the tip of Au NSs and the large number of high-density hot spots generated between adjacent Au-NSs on the GO surfaces; (ii) LSPR effect between Au nanocrystals on the surfaces of capture probes; (iii) the double signal enhancement caused by the plasmon coupling of capture probes and SERS tags and (iv) the increased hot spots density produced by magnet-assisted enrichment of sandwich-like SERS active substrates. Furthermore, in practical applications, SERS platform was successfully used for detecting *E. coli* and *S. aureus* in milk samples with recovery rates from 92.8 % to 111.1 % and 91.2 % to 104.9 %, and the RSD values in the range of 4.3 % to 5.0 % and 3.5 % to 6.9 %, respectively. Therefore, our research not only offers new avenues to simultaneously detect multiple pathogens, but also opens the door to countless possibilities in ensuring food safety to protect public health.

CRediT authorship contribution statement

Wenshi Zhao: Conceptualization, Formal analysis, Methodology, Investigation. **Shuo Yang:** Investigation. **Daxin Zhang:** Software. **Tianxiang Zhou:** Validation, Supervision. **Jie Huang:** Software. **Ming Gao:** Validation. **Yuhong Jiang:** Investigation. **Yang Liu:** Resources, Supervision, Writing – review & editing. **Jinghai Yang:** Resources, Supervision.

Data availability

No data was used for the research described in the article.

Declaration of Competing Interest

The authors declare that they have no known competing financial interests or personal relationships that could have appeared to influence the work reported in this paper.

Acknowledgements

Appendix A. Supplementary material

Supplementary data to this article can be found online at https://doi.org/10.1016/j.jcis.2022.12.077.

References

[1] Y. Pang, N. Wan, L. Shi, C. Wang, Z. Sun, R. Xiao, S. Wang, Dual-recognition surface-enhanced Raman scattering (SERS) biosensor for pathogenic bacteria detection by using vancomycin-SERS tags and aptamer-Fe$_3$O$_4$@Au, Anal. Chim. Acta 1077 (2019) 288–296.

[2] K. Yuan, Q. Mei, X. Guo, Y. Xu, D. Yang, B.J. Sánchez, B. Sheng, C. Liu, Z. Hu, G. Yu, H. Ma, H. Gao, C. Haisch, R. Niessner, Z. Jiang, H. Zhou, Antimicrobial peptide based magnetic recognition elements and Au@Ag-GO SERS tags with stable internal standards: a three in one biosensor for isolation, discrimination and killing of multiple bacteria in whole blood, Chem. Sci. 9 (2018) 8781–8795.

[3] Y. Wang, H. Ni, H. Li, J. Chen, D. Zhang, L. Fu, Plasmonic microneedle arrays for rapid extraction, SERS detection, and inactivation of bacteria, Chem. Eng. J. 442 (2022) 136140.

[4] Z. Feng, T. Tang, T. Wu, X. Yu, Y. Zhang, M. Wang, J. Zheng, Y. Ying, S. Chen, J. Zhou, X. Fan, D. Zhang, S. Li, M. Zhang, J. Qian, Perfecting and extending the near-infrared imaging window, Light-Sci. Appl. 10 (2021) 197.

[5] F. Sahin, N. Celik, A. Ceylan, S. Pekdemir, M. Ruzi, M.S. Onses, Antifouling superhydrophobic surfaces with bactericidal and SERS activity, Chem. Eng. J. 431 (2022) 133445.

[6] W. Zhao, D. Zhang, T. Zhou, J. Huang, Y. Wang, B. Li, L. Chen, J. Yang, Y. Liu, Aptamer-conjugated magnetic Fe$_3$O$_4$@Au core-shell multifunctional nanoprobe: A three-in-one aptasensor for selective capture, sensitive SERS detection and efficient near-infrared light triggered photothermal therapy of Staphylococcus aureus, Sensor. Actuat. B-Chem. 350 (2022) 130879.

[7] C. Zhang, C. Wang, R. Xiao, L.i. Tang, J. Huang, D.i. Wu, S. Liu, Y. Wang, D. Zhang, S. Wang, X. Chen, Sensitive and specific detection of clinical bacteria via vancomycin-modified Fe$_3$O$_4$@Au nanoparticles and aptamer-functionalized SERS tags, J. Mater. Chem. B 6 (22) (2018) 3751–3761.

[8] H. Shang, M. Ding, X. Zhang, W. Zhang, Dual-mode biosensing platform for sensitive and portable detection of hydrogen sulfide based on cuprous oxide/gold/copper metal organic framework heterojunction, J. Colloid Interf. Sci. 629 (2023) 796–804.

[9] H. He, D.W. Sun, H. Pu, L. Huang, Bridging Fe$_3$O$_4$@Au nanoflowers and Au@Ag nanospheres with aptamer for ultrasensitive SERS detection of aflatoxin B1, Food Chem. 324 (2020) 126832.

[10] H. Zhang, X. Ma, Y. Liu, N. Duan, S. Wu, Z. Wang, B. Xu, Gold nanoparticles enhanced SERS aptasensor for the simultaneous detection of Salmonella typhimurium and Staphylococcus aureus, Biosens. Bioelectron. 74 (2015) 872–877.

[11] M. Rubab, H.M. Shahbaz, A.N. Olaimat, D.H. Oh, Biosensors for rapid and sensitive detection of Staphylococcus aureus in food, Biosens. Bioelectron. 105 (2018) 49–57.

[12] J. Chen, J. Yang, W. Chen, Y. Wang, G. Song, H. He, H. Wang, P. Li, G.P. Wang, Tri-functional SERS nanoplatform with tunable plasmonic property for synergistic antibacterial activity and antibacterial process monitoring, J. Colloid Interf. Sci. 608 (2022) 2266–2277.

[13] Z. Chen, M. Segev, Highlighting photonics: looking into the next decade, eLight 1 (2021) 2.

[14] P. Qi, Y. Luo, B. Shi, W. Li, D. Liu, L. Zheng, Z. Liu, Y. Hou, Z. Fang, Phonon scattering and exciton localization: molding exciton flux in two dimensional disorder energy landscape, eLight 1 (2021) 6.

[15] Q. Bai, H. Luo, S. Shi, S. Liu, L. Wang, F. Du, Z. Yang, Z. Zhu, N. Sui, AuAg nanocages/graphdiyne for rapid elimination and detection of trace pathogenic bacteria, J. Colloid Interf. Sci. 613 (2022) 376–383.

[16] J. Xiong, S.-T. Wu, Planar liquid crystal polarization optics for augmented reality and virtual reality: from fundamentals to applications, eLight 1 (2021) 3.

[17] D. Lee, S. So, G. Hu, M. Kim, T. Badloe, H. Cho, J. Kim, H. Kim, C.-W. Qiu, J. Rho, Hyperbolic metamaterials: fusing artificial structures to natural 2D materials, eLight 2 (2022) 1.

[18] B. Xiao, G.N. Rutherford, A.P. Sharma, S.K. Pradhan, C.E. Bonner, M.J. Bahoura, Surface Modification and Charge Injection in a Nanocomposite Of Metal Nanoparticles and Semiconductor Oxide Nanostructures, Sci. Rep. 10 (2020) 4743.

[19] M. Richard-Lacroix, V. Deckert, Direct molecular-level near-field plasmon and temperature assessment in a single plasmonic hotspot, Light-Sci. Appl. 9 (2020) 35.

[20] S. Park, J. Lee, H. Ko, Transparent and Flexible Surface-Enhanced Raman Scattering (SERS) Sensors Based on Gold Nanostar Arrays Embedded in Silicon Rubber Film, ACS Appl. Mater. Inter. 9 (50) (2017) 44088–44095.

[21] B. Zhao, R. Hao, Z. Wang, H. Zhang, Y. Hao, C. Zhang, Y. Liu, Green synthesis of multi-dimensional plasmonic coupling structures: Graphene oxide gapped gold nanostars for highly intensified surface enhanced Raman scattering, Chem. Eng. J. 349 (2018) 581–587.

[22] R. Prucek, A. Panacek, Z. Gajdova, R. Vecerova, L. Kvitek, J. Gallo, M. Kolar, Specific detection of Staphylococcus aureus infection and marker for Alzheimer disease by surface enhanced Raman spectroscopy using silver and gold nanoparticle-coated magnetic polystyrene beads, Sci. Rep. 11 (2021) 6240.

[23] X. Yu, Y. Zhong, Y.u. Sun, Y. Chen, Controllable Preparation of Plasmonic Gold Nanostars for Enhanced Photothermal and SERS Effects, Chem. Res. Chinese U. 36 (6) (2020) 1284–1291.

[24] X.-B. Huang, S.-H. Wu, H.-C. Hu, J.-J. Sun, AuNanostar@4-MBA@Au Core-Shell Nanostructure Coupled with Exonuclease III-Assisted Cycling Amplification for Ultrasensitive SERS Detection of Ochratoxin A, ACS Sens. 5 (8) (2020) 2636–2643.

[25] A. Li, L. Tang, D. Song, S. Song, W. Ma, L. Xu, H. Kuang, X. Wu, L. Liu, X. Chen, C. Xu, SERS-active sensor based on heterogeneous gold nanostar core-silver nanoparticle satellite assemblies for ultrasensitive detection of aflatoxinB1, Nanoscale 8 (2016) 1873–1878.

[26] L. Xu, H. Zhang, Y. Tian, A. Jiao, S. Li, Y. Tan, M. Chen, F. Chen, Modified photochemical strategy to support highly-purity, dense and monodisperse Au nanospheres on graphene oxide for optimizing SERS detection, Talanta 209 (2020) 120535.

[27] H. Tang, T. Yang, L. Chen, Y. Zhang, Y. Zhu, C. Wang, D. Liu, Q. Guo, G. Cheng, F. Xia, T. Zhong, J. Wang, Surface chemistry of graphene tailoring the activity of digestive enzymes by modulating interfacial molecular interactions, J. Colloid Interf. Sci. 630 (2023) 179–192.

[28] X. Meng, H. Wang, N. Chen, P. Ding, H. Shi, X. Zhai, Y. Su, Y. He, A Graphene-Silver Nanoparticles-Silicon Sandwich SERS Chip for Quantitative Detection of Molecules and Capture, Discrimination, Inactivation of Bacteria, Anal. Chem. 90 (2018) 5646–5653.

[29] Y. Tong, Q. Zhou, Y. Sun, X. Sheng, B. Zhou, J. Zhao, J. Guo, Magnetic polyamidoamine dendrimer grafted with 4-mercaptobenzoic acid as an adsorbent for preconcentration and sensitive determination of polycyclic aromatic hydrocarbons from environmental water samples, Talanta 224 (2021) 121884.

[30] G. Cattani, A. Bocedi, G. Gambardella, F. Iavarone, M. Boroumand, M. Castagnola, G. Ricci, Trypsinogen and chymotrypsinogen: the mysterious hyper-reactivity of selected cysteines is still present after their divergent evolution, FEBS J. 288 (2021) 6003–6018.

[31] Z. Hu, X. Zhou, J. Duan, X. Wu, J. Wu, P. Zhang, W. Liang, J. Guo, H. Cai, P. Sun, H. Zhou, Z. Jiang, Aptamer-based novel Ag-coated magnetic recognition and SERS nanotags with interior nanogap biosensor for ultrasensitive detection of protein biomarker, Sensor. Actuat. B-Chem. 334 (2021) 129640.

[32] S. Yin, E. Galiffi, A. Alù, Floquet metamaterials 2 (eLight 2022,) 8.

[33] X. Wang, M. Wang, T. Jiang, F. Wang, Y. Qing, S. Bu, J. Zhou, Dual-functional Fe$_3$O$_4$@SiO$_2$@Ag triple core-shell microparticles as an effective SERS platform for adipokines detection, Colloid. Surface. A. 535 (2017) 24–33.

[34] W. Zhao, S. Yang, C. Guo, J. Yang, Y. Liu, One-step fabrication of Fe$_3$O$_4$-Cu nanocomposites: High-efficiency and low-cost catalysts for reduction of 4-nitrophenol, Mater. Chem. Phys. 260 (2021) 124144.

[35] J. Huang, T. Zhou, W. Zhao, S. Cui, R. Guo, D. Li, N. Reddy Kadasala, D. Han, Y. Jiang, Y. Liu, H. Liu, Multifunctional magnetic Fe$_3$O$_4$/Cu$_2$O-Ag nanocomposites with high sensitivity for SERS detection and efficient visible light-driven photocatalytic degradation of polycyclic aromatic hydrocarbons (PAHs), J. Colloid Interf. Sci. 628 (2022) 315–326.

[36] S.-M. You, K.e. Luo, J.-Y. Jung, K.-B. Jeong, E.-S. Lee, M.-H. Oh, Y.-R. Kim, Gold Nanoparticle-Coated Starch Magnetic Beads for the Separation, Concentration, and SERS-Based Detection of E. coli O157: H7, ACS Appl. Mater. Inter. 12 (16) (2020) 18292–18300.

[37] Z. Zhou, R. Xiao, S. Cheng, S. Wang, L. Shi, C. Wang, K. Qi, S. Wang, A universal SERS-label immunoassay for pathogen bacteria detection based on Fe$_3$O$_4$@Au-aptamer separation and antibody-protein A orientation recognition, Anal. Chim. Acta 1160 (2021) 338421.

[38] J. Chen, S. Pang, L. He, S.R. Nugen, Highly sensitive and selective detection of nitrite ions using Fe$_3$O$_4$@SiO$_2$/Au magnetic nanoparticles by surface-enhanced Raman spectroscopy, Biosens. Bioelectron. 85 (2016) 726–733.

[39] T. Wu, H. Zheng, Y. Kou, X. Su, N.R. Kadasala, M. Gao, L. Chen, D. Han, Y. Liu, J. Yang, Self-sustainable and recyclable ternary Au@Cu$_2$O-Ag nanocomposites: application in ultrasensitive SERS detection and highly efficient photocatalysis of organic dyes under visible light, Microsyst. Nanoeng. 7 (2021) 23.

[40] D.C. Marcano, D.V. Kosynkin, J.M. Berlin, A. Sinitskii, Z. Sun, A. Slesarev, L.B. Alemany, W. Lu, J.M. Tour, Improved Synthesis of Graphene Oxide, ACS Nano 4 (8) (2010) 4806–4814.

[41] X. Pan, L. Li, H. Lin, J. Tan, H. Wang, M. Liao, C. Chen, B. Shan, Y. Chen, M. Li, A graphene oxide-gold nanostar hybrid based-paper biosensor for label-free SERS detection of serum bilirubin for diagnosis of jaundice, Biosens. Bioelectron. 145 (2019) 111713.

[42] S. Cheng, Z. Tu, S. Zheng, X. Cheng, H. Han, C. Wang, R. Xiao, B. Gu, An efficient SERS platform for the ultrasensitive detection of Staphylococcus aureus and Listeria monocytogenes via wheat germ agglutinin-modified magnetic SERS substrate and streptavidin/aptamer co-functionalized SERS tags, Anal. Chim. Acta 1187 (2021) 339155.

[43] S. Sadighian, K. Rostamizadeh, H. Hosseini-Monfared, M. Hamidi, Doxorubicin-conjugated core-shell magnetite nanoparticles as dual-targeting carriers for anticancer drug delivery, Colloid. Surface. B. 117 (2014) 406–413.

[44] H. Jiang, X. Zeng, Z. Xi, M. Liu, C. Li, Z. Li, L. Jin, Z. Wang, Y. Deng, N. He, Improvement on controllable fabrication of streptavidin-modified three-layer core-shell $Fe_3O_4@SiO_2@Au$ magnetic nanocomposites with low fluorescence background, J. Biomed. Nanotechnol. 9 (2013) 674–684.

[45] D.A. Wheeler, S.A. Adams, T. López-Luke, A. Torres-Castro, J.Z. Zhang, Magnetic Fe_3O_4-Au core-shell nanostructures for surface enhanced Raman scattering, Ann. Phys-Berlin 524 (2012) 670–679.

[46] M.E. Khosroshahi, L. Ghazanfari, Physicochemical characterization of $Fe_3O_4/SiO_2/Au$ multilayer nanostructure, Mater. Chem. Phys. 133 (1) (2012) 55–62.

[47] C. Zhang, C. Li, J. Yu, S. Jiang, S. Xu, C. Yang, Y.J. Liu, X. Gao, A. Liu, B. Man, SERS activated platform with three-dimensional hot spots and tunable nanometer gap, Sensor. Actuat. B-Chem. 258 (2018) 163–171.

[48] Y. Kou, T. Wu, H. Zheng, N.R. Kadasala, S. Yang, C. Guo, L. Chen, Y. Liu, J. Yang, Recyclable Magnetic MIP-Based SERS Sensors for Selective, Sensitive, and Reliable Detection of Paclobutrazol Residues in Complex Environments, ACS Sustain. Chem. Eng. 8 (38) (2020) 14549–14556.

[49] S. Diaz-Amaya, L.K. Lin, A.J. Deering, L.A. Stanciu, Aptamer-based SERS biosensor for whole cell analytical detection of E. coli O157: H7, Anal. Chim. Acta (2019, 1081,) 146–156.

[50] D. Cheng, M. Yu, F. Fu, W. Han, G. Li, J. Xie, Y. Song, M.T. Swihart, E. Song, Dual Recognition Strategy for Specific and Sensitive Detection of Bacteria Using Aptamer-Coated Magnetic Beads and Antibiotic-Capped Gold Nanoclusters, Anal. Chem. 88 (1) (2016) 820–825.

[51] N. Deng, B. Jiang, Y.C. Liang, L. Zhang, Y. Liang, K. Yang, Y. Zhang, Aptamer-conjugated gold functionalized graphene oxide nanocomposites for human a-thrombin specific recognition, J. Chromatogr. A 1427 (2016) 16–21.

[52] C. Wang, J. Wang, M. Li, X. Qu, K. Zhang, Z. Rong, R. Xiao, S. Wang, A rapid SERS method for label-free bacteria detection using polyethylenimine-modified Au-coated magnetic microspheres and Au@Ag nanoparticles, Analyst 141 (22) (2016) 6226–6238.

[53] C. Wang, B. Gu, Q. Liu, Y. Pang, R. Xiao, S. Wang, Combined use of vancomycin-modified Ag-coated magnetic nanoparticles and secondary enhanced nanoparticles for rapid surface-enhanced Raman scattering detection of bacteria, Int. J. Nanomed. 13 (2018) 1159–1178.

[54] M.M. Hassan, Q. Chen, F.Y.H. Kutsanedzie, H. Li, M. Zareef, Y.i. Xu, M. Yang, A.A. Agyekum, rGO-NS SERS-based coupled chemometric prediction of acetamiprid residue in green tea Author links open overlay panel, J. Food Drug Anal. 27 (1) (2019) 145–153.

[55] X. Shi, Y. Xu, B. Zhao, P. Li, M. Song, J. Jia, H. Yu, G. Lu, Integrating Conductive Metal-Organic Framework with Graphene Oxide to Highly Sensitive Platform for Electrochemical Sensing, Adv. Mater. Interfaces 8 (2021) 2100586.

[56] H. Zheng, D. Ni, Z. Yu, P. Liang, Preparation of SERS-active substrates based on graphene oxide/silver nanocomposites for rapid zdetection of l-Theanine, Food Chem. 217 (2017) 511–516.

[57] Y. Luan, S. Tang, Z. Wang, Y. Li, The effect of MoS_2 coating on localized surface plasmon resonance of Au/Ag nano particles, Photonic. Nanostruct. 47 (2021) 100970.

[58] K.K. Reza, S. Dey, A. Wuethrich, W. Jing, A. Behren, F. Antaw, Y. Wang, A.A. Sina, M. Trau, In Situ Single Cell Proteomics Reveals Circulating Tumor Cell Heterogeneity during Treatment, ACS Nano 15 (2021) 11231–11243.

[59] Y. Hang, J. Boryczka, N. Wu, Visible-light and near-infrared fluorescence and surface-enhanced Raman scattering point-of-care sensing and bio-imaging: a review, Chem. Soc. Rev. 51 (1) (2022) 329–375.

[60] C. Wang, C. Wang, X. Wang, K. Wang, Y. Zhu, Z. Rong, W. Wang, R. Xiao, S. Wang, Magnetic SERS Strip for Sensitive and Simutaneous Detection of Respiratory Viruses, ACS Appl. Mater. Inter. 11 (2019) 19495–19505.

[61] A. Ecija-Arenas, E.M. Kirchner, T. Hirsch, J.M. Fernandez-Romero, Development of an aptamer-based SPR-biosensor for the determination of kanamycin residues in foods, Anal. Chim. Acta 1169 (2021) 338631.

[62] R. Pardehkhorram, F. Alshawawreh, V.R. Goncales, N.A. Lee, R.D. Tilley, J.J. Gooding, Functionalized Gold Nanorod Probes: A Sophisticated Design of SERS Immunoassay for Biodetection in Complex Media, Anal. Chem. 93 (2021) 12954–12965.

[63] Y. Zhang, Y. Huang, Z. Yue, H. Fan, S. Wu, Preparation and application of aptamer-functionalized sorbent for the analysis of ultra-trace aflatoxin M1 and analogues in milk, Microchem. J. 166 (2021) 106179.

[64] J. Jagiełło, M. Kuśmierz, E. Kijeńska-Gawrońska, M. Winkowska-Struzik, W. Święszkowski, L. Lipińska, Adhesive properties of graphene oxide and its modification with RGD peptide towards L929 cells, Mater. Today Commun. 26 (2021) 102056.

[65] C. Zhu, Q. Zhao, X. Wang, Z. Li, X. Hu, Ag-nanocubes/graphene-oxide/Au-nanoparticles composite film with highly dense plasmonic hotspots for surface-enhanced Raman scattering detection of pesticide, Microchem. J. 165 (2021) 106090.

[66] N. Riswana Barveen, T.-J. Wang, Y.-H. Chang, Photochemical synthesis of Au nanostars on PMMA films by ethanol action as flexible SERS substrates for in-situ detection of antibiotics on curved surfaces, Chem. Eng. J. 431 (2022) 134240.

[67] Q. Wang, J. Li, Y. Song, L. Duan, C. Yan, L. Qu, Y. Wu, C. Han, Graphene-embedded oblique V-shaped silver nanoarrays for hydrophobic pollutants pre-concentration and high-sensitivity SERS detection, J. Hazard. Mater. 426 (2022) 128085.

[68] Y.u. Han, X. Fang, Z. Sun, C. Kang, L. Zha, X. Zhang, Ag Nanoparticle-Decorated Graphene Oxide Coatings on the Inner Walls of Optofluidic Capillaries for Real-Time Trace SERS Detection, ACS Appl. Nano Mater. 5 (2) (2022) 2445–2450.

[69] K. Ponlamuangdee, G.L. Hornyak, T. Bora, S. Bamrungsap, Graphene oxide/gold nanorod plasmonic paper-a simple and costeffective SERS substrate for anticancer drug analysis, New J. Chem. 44 (33) (2020) 14087–14094.

[70] S. Yang, J. Yao, Y. Quan, M. Hu, R. Su, M. Gao, D. Han, J. Yang, Monitoring the charge-transfer process in a Nd-doped semiconductor based on photoluminescence and SERS technology, Light-Sci. Appl. 9 (2020) 117.

[71] D. Song, R. Yang, S. Fang, Y. Liu, F. Long, A. Zhu, SERS based aptasensor for ochratoxin A by combining Fe3O4@Au magnetic nanoparticles and Au-DTNB@Ag nanoprobes with multiple signal enhancement, Microchim. Acta 185 (2018) 491.

[72] A. Zhu, T. Jiao, S. Ali, Y.i. Xu, Q. Ouyang, Q. Chen, SERS Sensors Based on Aptamer-Gated Mesoporous Silica Nanoparticles for Quantitative Detection of Staphylococcus aureus with Signal Molecular Release, Anal. Chem. 93 (28) (2021) 9788–9796.

[73] X. Bai, A. Shen, J. Hu, A sensitive SERS-based sandwich immunoassay platform for simultaneous multiple detection of foodborne pathogens without interference, Anal. Methods 12 (40) (2020) 4885–4891.

[74] A. Zhu, S. Ali, Y. Xu, Q. Ouyang, Q. Chen, A SERS aptasensor based on AuNPs functionalized PDMS film for selective and sensitive detection of Staphylococcus aureus, Biosens. Bioelectron. 172 (2021) 112806.